



Originally published as:

Hainzl, S., Fischer, T., Čermáková, H., Bachura, M., Vlček, J. (2016): Aftershocks triggered by fluid-intrusion: Evidence for the aftershock sequence occurred 2014 in West Bohemia/Vogtland. - *Journal of Geophysical Research*, 121, 4, pp. 2575–2590.

DOI: <http://doi.org/10.1002/2015JB012582>

**Journal of Geophysical Research: Solid Earth****RESEARCH ARTICLE**

10.1002/2015JB012582

**Key Points:**

- Three aftershock sequences occurred after 30 years of swarms on the same fault plane
- Mainshocks activated a fault jog and had oblique mechanisms compared to aftershocks
- Mainshock-triggered fluid intrusion explains observed earthquake migration and high activity rates

**Correspondence to:**S. Hainzl,  
hainzl@gfz-potsdam.de**Citation:**

Hainzl, S., T. Fischer, H. Čermáková, M. Bachura, and J. Vlček (2016), Aftershocks triggered by fluid intrusion: Evidence for the aftershock sequence occurred 2014 in West Bohemia/Vogtland, *J. Geophys. Res. Solid Earth*, 121, 2575–2590, doi:10.1002/2015JB012582.

Received 5 OCT 2015

Accepted 18 MAR 2016

Accepted article online 22 MAR 2016

Published online 12 APR 2016

## Aftershocks triggered by fluid intrusion: Evidence for the aftershock sequence occurred 2014 in West Bohemia/Vogtland

S. Hainzl<sup>1</sup>, T. Fischer<sup>2,3</sup>, H. Čermáková<sup>3</sup>, M. Bachura<sup>2</sup>, and J. Vlček<sup>2</sup>

<sup>1</sup>GFZ German Research Centre for Geosciences, Potsdam, Germany, <sup>2</sup>Faculty of Science, Charles University, Prague, Czech Republic, <sup>3</sup>Institute of Geophysics, Czech Academy of Sciences, Prague, Czech Republic

**Abstract** The West Bohemia/Vogtland region, central Europe, is well known for its repeating swarm activity. However, the latest activity in 2014, although spatially overlapping with previous swarm activity, consisted of three classical aftershock sequences triggered by  $M_L$  3.5, 4.4, and 3.5 events. To decode the apparent system change from swarm-type to mainshock-aftershock characteristics, we have analyzed the details of the major  $M_L$  4.4 sequence based on focal mechanisms and relocated earthquake data. Our analysis shows that the mainshock occurred with rotated mechanism in a step over region of the fault plane, unfavorably oriented to the regional stress field. Most of its intense aftershock activity occurred in-plane with classical characteristics such as (i) the maximum magnitude of the aftershocks is significantly less than the mainshock magnitude and (ii) the decay can be well fitted by the Omori-Utsu law. However, the absolute number of aftershocks and the fitted Omori-Utsu  $c$  and  $p$  parameters are much larger than for typical sequences. By means of the epidemic-type aftershock sequence model, we show that an additional aseismic source with an exponentially decaying strength triggered a large fraction of the aftershocks. Corresponding pore pressure simulations with an exponentially decreasing flow rate of the fluid source show a good agreement with the observed spatial migration front of the aftershocks extending approximately with  $\log(t)$ . Thus, we conclude that the mainshock opened fluid pathways from a finite fluid source into the fault plane explaining the unusual high rate of aftershocks, the migration patterns, and the exponential decrease of the aseismic signal.

### 1. Introduction

Earthquake swarms, as specific type of seismic sequences, are characterized by close clustering in time and space and missing dominant events. Instead, several earthquakes of similarly large magnitudes occur so that smaller events are not associated with any identifiable mainshock. Earthquake swarms consist mostly of earthquakes occurring within several hours to several months at varying tectonic environments, both at boundaries of the lithospheric plates and within the plates. The absence of a dominating large event in seismic swarms is usually attributed to the heterogeneity of the stress field and/or weakened crust, which lacks a single well-developed fault and is incapable of sustaining higher strain [Mogi, 1963]. A large group of earthquake swarms is related to volcanic activity, but others appear as of purely tectonic origin [Horálek *et al.*, 2015]. As a result, two types of driving force of seismic swarms have been suggested: fluid pressure increase due to migration of magma and other crustal fluids [e.g., Duverger *et al.*, 2015; Shelly *et al.*, 2015] and stress changes associated to aseismic slip [e.g., Vidale and Shearer, 2006; Lohman and McGuire, 2007].

In contrast to earthquake swarms, typical earthquake clusters occurring at plate boundaries are mainshock-aftershock sequences initiated by a single mainshock, with a magnitude typically one or more magnitude units higher than those of the aftershocks (Båth law) [Båth, 1965]. The tectonic environment of aftershock sequences predestinates their driving force, which is the elastic stress readjustment in the area of mainshock [Lay and Wallace, 1995]. The aftershock rate  $R$  generally decays according to the Omori-Utsu law,

$$R(t) = K_0(c + t)^{-p}, \quad (1)$$

where  $t$  is the elapsed time since the mainshock and  $K_0$ ,  $c$ , and  $p$  are constants; see Utsu *et al.* [1995] for a review. The exponent  $p$  is mostly in the range of 0.8–1.2, and  $K_0$  is known to depend exponentially on  $M$  [Utsu *et al.*, 1995; Hainzl and Marsan, 2008]. Detailed aftershock studies showed that the delay parameter  $c$

is very small, in the order of one to several minutes or even less [e.g., Peng *et al.*, 2006; Enescu *et al.*, 2007; Lengliné and Ampuero, 2015], while larger estimations often result from incomplete recordings directly after the occurrence of larger earthquakes [Kagan, 2004]. The Omori-Utsu law has been explained, among others, by the mainshock-induced (i) poroelastic response [Nur and Booker, 1972], (ii) afterslip [Perfettini and Avouac, 2004], or (iii) delayed earthquake nucleation due to rate- and state-dependent friction [Dieterich, 1994; Stein, 1999]. The release of pressurized fluids by the mainshock may also contribute to driving aftershock activity as documented by Miller *et al.* [2004] for the 1997 Umbria-Marche seismic sequence in North Appenines, Italy.

Earthquake swarms and mainshock-aftershock sequences usually show exclusive occurrence; in some cases they occur in parallel at broader areas, similarly to the Central Apennines where the year 2009  $M_w$  6.3 L'Aquila earthquake was followed by a swarm in the NW direction from the mainshock [Chiaraluce, 2012]. Swarms sometimes also precede large earthquakes like the  $M$  7.3 Tottori earthquake in 2000 that was preceded by swarms in 1989, 1990, and 1997 whose hypocenters lied at the fault plane of future mainshock [Ohmi *et al.*, 2002]. Partially similar to our studied area, a  $M_w$  4.1 mainshock occurred in 2012 in French Alps, 10 km from the area activated by the preceding 2003–2004 Ubaye swarm [Courboulex *et al.*, 2013].

Our study deals with the mainshock-aftershock sequences that occurred 2014 in the West Bohemia/Vogtland region of Central Europe. Hypocenters of the 2014 mainshock-aftershock activity significantly overlap with the hypocenters of swarms that occurred within the previous 30 years on the same fault patch. West Bohemia/Vogtland is an intraplate region which was previously only characterized by repeated occurrence of earthquake swarms and degassing of CO<sub>2</sub> of upper mantle origin [Fischer *et al.*, 2014]. This region is located at an intersection of two regional tectonic structures: NE-SW trending Eger Rift and NNW-SSE trending Mariánské Lázně Fault (Figure 1). Instrumental observations started in early 1960, which were replaced by permanent digital recording at early 1990 since when precise hypocenter locations are available [Fischer *et al.*, 2014]. The seismicity from this period is distributed within a N-S elongated area of 60 × 110 km extent and concentrates in the zone of Nový Kostel (indicated by a rectangle in Figure 1). In this time period, six  $M_L$  3+ earthquake sequences have occurred in this zone: swarms in 1985/1986 (maximum  $M_L$  of 4.6), 1997, 2000, 2008, 2011, and the most recent sequence in 2014 with maximum  $M_L$  of 4.4. Although the activity before 2014 included some embedded mainshock-aftershock sequences [Hainzl and Fischer, 2002], previous sequences showed overall typical swarm characteristics. In contrast, the activity in 2014 consisted of three classical mainshock-aftershock sequences related to mainshocks with local magnitude of 3.5 (24 May), 4.4 (31 May), and 3.5 (3 August) which triggered Omori-Utsu-type aftershock activity. On top of the nonswarm character of these sequences, their hypocenter locations overlapped significantly with the hypocenters of previous swarms (Figure 1), which opens the question of the generating mechanisms of the earthquakes, which creates either swarms or mainshocks at the same fault segment. To reveal the underlying processes, we analyze in this study the focal zone geometry, source mechanisms, and the spatiotemporal evolution of the most intense mainshock-aftershock sequence related to the largest  $M_L$  4.4 event.

## 2. Earthquake Data and Processing

We used data recorded by the WEBNET seismic network that consists of 13 telemetered and 9 autonomous seismic stations sampled at 250 Hz with seismograms proportional to the ground velocity in the frequency band of at least 1–80 Hz [Fischer *et al.*, 2010]. The analyzed seismic catalog of the 2014 activity was obtained by supplementing the manually processed data with automatic picks provided by the Pepin picker and locator. It is based on the method of Fischer [2003a, 2003b], which is implemented at WEBNET real-time preprocessing (<http://ig.cas.cz/en/structure/observatories/west-bohemia-seismic-network-webnet/map-epicenters>). The automatic and manual catalogs were combined using the criterion of unique origin times. The precision of arrival time measurements and related location quality were homogenized by delay times for pairs of events measured using cross-correlation technique and double-difference relocation. To this purpose, waveforms were filtered to a frequency band 1–10 Hz (three-pole Butterworth band-pass filter) or 1–7 Hz when an event with magnitude higher than  $M_L$  3 occurred in the correlated event pair. Time intervals of 1 s and 1.5 s duration centered at the measured  $P$  and  $S$  arrival times, respectively, were trimmed and cross correlated to obtain absolute arrival time difference for  $P$  and  $S$  waves. Resulting arrival time differences along with the cross-correlation coefficients as weighting factors were used as inputs for hypoDD relocation [Waldauser and Ellsworth, 2000; Waldauser, 2001]. As a result, the combined 2014 catalog comprised 3757 relocated events of which 1902 were processed manually and 1855 automatically; the automatically obtained events contributed only to the magnitude level below  $M_L$  1.8.

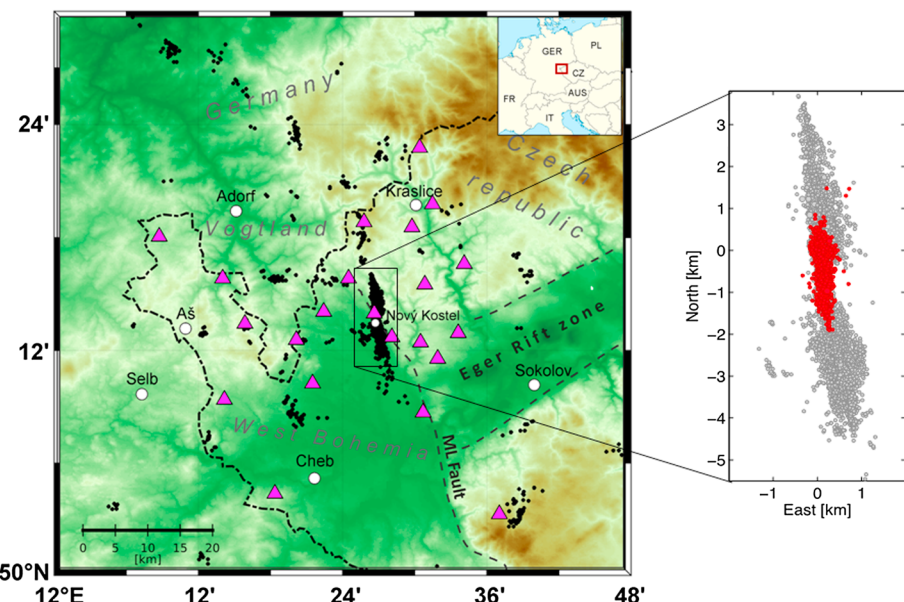


**Figure 1.** The area of West Bohemia Vogtland; rectangle indicates the Nový Kostel zone with dominating seismic activity. The 2014 hypocenters are indicated by red; the hypocenters of previous swarms are gray, and triangles refer to the seismic stations of the WEBNET.

Focal mechanisms of the 2014 activity were determined by the AMT code [Vavryčuk, 2009] that inverts the  $P$  wave amplitudes for full moment tensor; here we use the double-couple part only. At least 14 stations were used for determining the focal mechanisms, and the stability of the solution was tested by omitting individual stations from the data set. We chose the optimum fault plane from the two nodal planes using the fault instability criterion [Vavryčuk, 2014], which is based on comparing the proximity of the stress state to the failure envelope in the Mohr-Coulomb diagram.

### 3. Results

Figure 2a shows the temporal evolution of the 2014 earthquake activity which started on 24 May 2014 at 14:35 UTC by a  $M_L$  3.5 earthquake occurring after a long period of quiescence; only two small events occurred in the Nový Kostel area within 1 week prior to this event, and no activity was observed few months before. This earthquake was followed by 170 aftershocks located in the near vicinity of the mainshock. The aftershock activity ceased after few hours followed by a period of relative quiescence until the second mainshock on 31 May 2014. This  $M_L$  4.4 earthquake was the largest in the sequence; it occurred at 10:37 UTC and was preceded by a single  $M_L$  1.3 foreshock 2 h ahead. Its aftershock sequence lasted for a week and involved almost 3000 located events. Sporadic seismic activity in the next 2 months culminated by the third mainshock on 3 August 2014, 23:58 UTC with  $M_L$  = 3.5, which was preceded by about 10  $M_L$  < 1 events occurred a few hours before and triggered itself about 440 aftershocks. The moment magnitudes were  $M_w$ , 3.4, 3.8, and 3.4 for the 24 May, 31 May, and 3 August mainshocks (V. Vavryčuk, personal communication and U.S. Geological Survey, 2015).

#### 3.1. Frequency-Magnitude Distribution

The frequency-magnitude distribution of the sequence is shown in Figure 3, indicating a Gutenberg-Richter distribution with a  $b$  value of approximately 1.2 for magnitudes  $M_L \geq 1$ , while the deviation for  $M_L < 1$  events might be related to partial incompleteness. In the same figure, the distribution is also shown for the aftershocks occurred in the first 10 days after the  $M_L$  4.4 mainshock. Here we ignored the first aftershocks, because of the typical incompleteness of earthquake catalogs directly after mainshocks [Kagan, 2004]. For  $M_L \geq 1$  events, the incompleteness period  $t$  is approximately 50 min for a mainshock of  $M = 4.4$  according to the empirical dependence of the completeness magnitude  $M_c$  on time (in days) and mainshock magnitude,  $M_c(M, t) = M - 4.5 - 0.75 \log(t)$ , derived for aftershock sequences in California [Helmstetter et al., 2006]. The frequency-magnitude distribution of the aftershocks is found to have a very similar trend as the overall distribution, indicating a completeness magnitude of at least  $M_c = 1.0$ . We use this conservative threshold

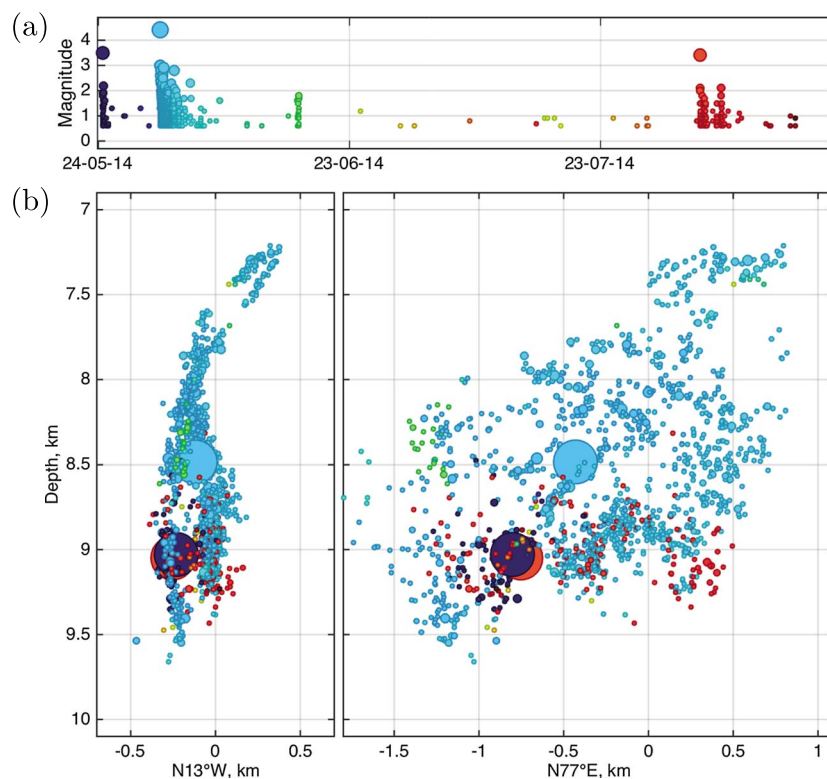


**Figure 2.** (a) Magnitude-time plot of the 2014 sequence and (b) two vertical sections oriented across and along the hypocenter trend, where symbol size is proportional to magnitude; the size of main shocks is exaggerated. Events are color coded according to their occurrence times.

for later model fits requiring complete data, while all events are used to study the spatial distribution and migration pattern. The resolved  $b$  value of 1.2 lies in the upper part of the  $b$  value interval reported for West-Bohemia/Vogtland swarms. The existing studies [e.g., Neuhöfer and Hemmann, 2005] found  $b$  values ranging from 0.5 to 1.5 with temporal variations; the most striking was probably the decrease of  $b$  from about 1.3 in the beginning of the 2000 swarm down to 0.8 in the second swarm period that was accompanied by the increase of the mean seismic moment [Hainzl and Fischer, 2002]. Hence, the 2014 mainshock-aftershock sequence is not anomalous in terms of the  $b$  value level, compared to the previous swarm-like seismicity.

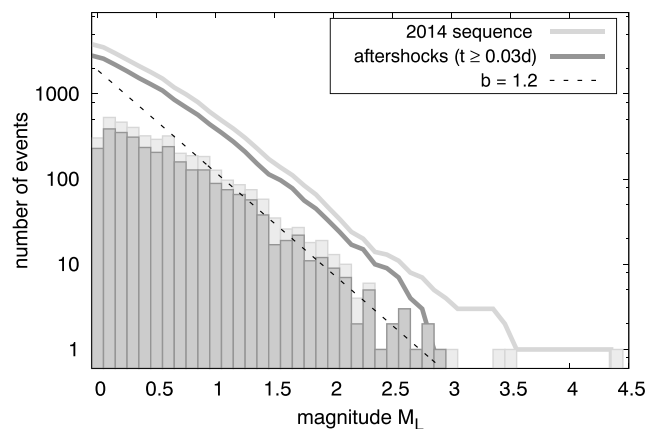


**Figure 3.** Frequency-magnitude distribution of the whole activity (light color) and the first 10 days of aftershock activity following the  $M_L 4.4$  event (dark color). The dashed line refers to a Gutenberg-Richter relation with  $b = 1.2$ . The bar diagram shows the corresponding histogram of the magnitudes.

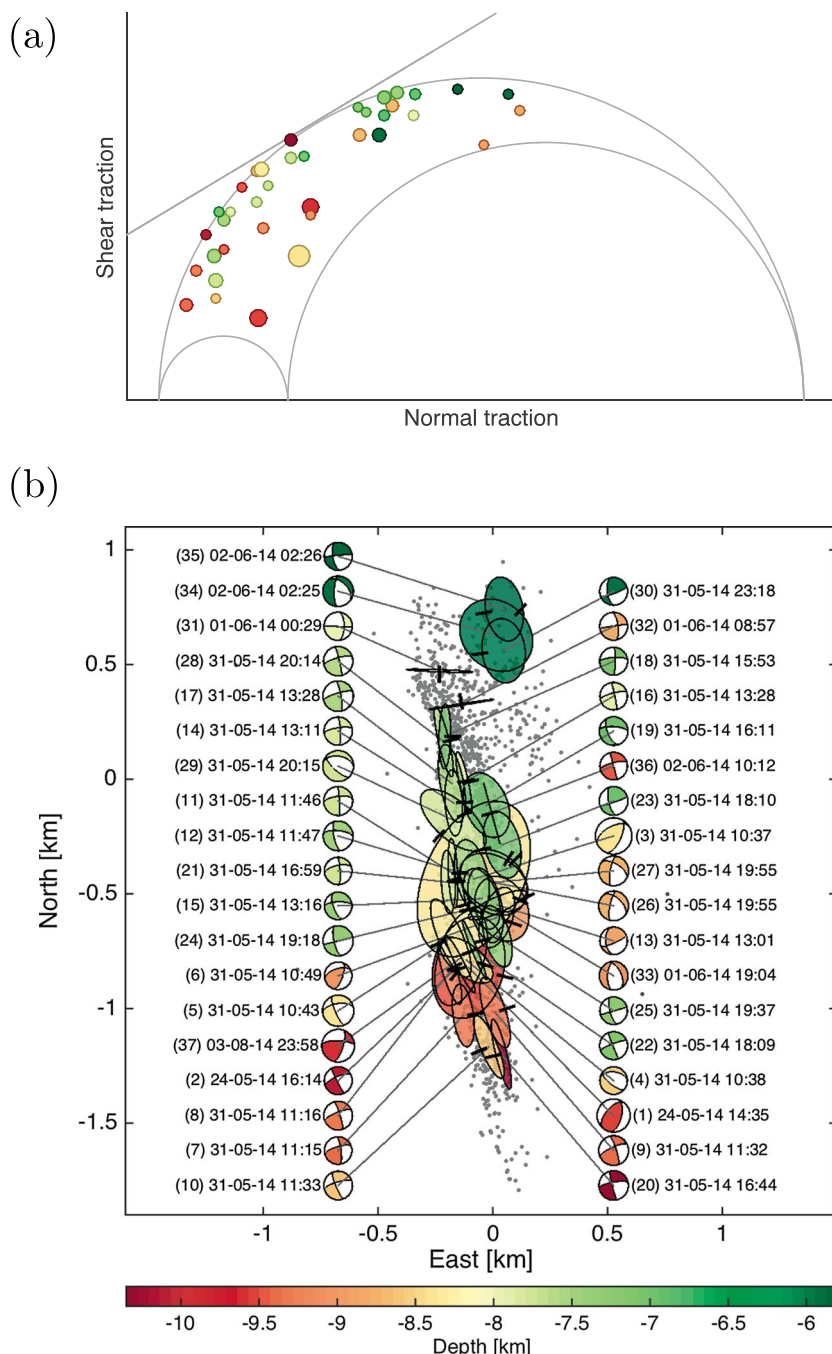


**Figure 4.** Source mechanisms of the  $M_L \geq 2$  events occurred during the sequence in the year 2014: (a) Mohr-Coulomb plot showing the shear and normal tractions resolved on the optimal fault planes indicated in Figure 5b; where a friction coefficient of 0.6 and the regional stress of Vavryčuk [2014] are assumed. Note that the fault planes of the three mainshocks (large red and yellow circles) are the most stable showing one of the largest perpendicular distances to the failure envelope. (b) Epicenters (gray points) and focal mechanisms, where the ellipses show the optimal fault planes selected by the instability criterion; their size is scaled with magnitude. Horizontal projection of circular rupture is shown with short line indicating the dip direction. Mainshocks are indicated by numbers 1, 3, and 37.

### 3.2. Spatial Distribution

The activity in 2014 occurred on an inclined planar structure within an oval area of  $2.5 \times 2.5$  km size centered at 8.5 km depth (Figure 2b). While the subsequences related to the two  $M_L = 3.5$  mainshocks occurred only in the deeper part of the plane, the aftershocks of the  $M_L 4.4$  event extended over the whole area. However, all

sequences activated two parallel clusters, which are separated by a gap of few hundred meters length, where the southern cluster was activated first followed by the northern cluster. The lower parts of the two clusters can be approximated by two subvertical planes with an offset of about 250 m. The mainshocks themselves occurred all near to this gap between the two clusters, less than 500 m apart from each other. The mainshocks thus appear to be related to the offset/jog of a preexisting fault plane. It is of interest that the first and last mainshock locations overlap which is verified by bootstrap estimates of the location error. It is hard to distinguish these two mainshock locations, while the largest  $M_L$  4.4 mainshock of 31 May has a clearly distinct position.

The focal mechanisms of  $M_L \geq 2$  events occurred during the largest sequence are quite self-similar with prevalence of oblique strike-slip events whose fault planes match the NNW-SSE trend of hypocenters (Figure 5b). The fit is, however, interrupted by the fault jog pronounced also in the offset of ellipses indicating the fault planes. Note that the whole Nový Kostel fault zone trends 169° [Fischer et al., 2014] with the typical strike of 355° and 164° for oblique normal events and oblique reverse events, respectively [Čermáková and Horálek, 2015], which is consistent with most of the 2014 focal mechanisms. It should be noted that the estimated source mechanisms of this sequence show negligible isotropic component of about 15%; however, their CLVD component ranges from 10 to 70%, which points to the possible inequality of the fault surfaces or inconsistency in the data or velocity model. Anyway, this would have no significant impact on our study, which is based on the more stable double-couple part represented by the angles of the fault planes. Despite the general homogeneity of the estimated focal mechanisms, a few events (1, 5, 8, 28, 29, 32, and 33) show anomalous solutions with different strike and a large normal or reverse component. These anomalous events include all the three mainshocks with preferred rupture planes striking 25–41° (dip = 56–65°, rake = 64–73°), which intersect the two parallel fault planes of the southern and northern clusters striking 347°.

Displacement spectra of three mainshocks were inverted for corner frequencies and station-specific attenuation using the approach of Michálek and Fischer [2013] (Figure 4). It appears that despite the different low-frequency level, the spectra are quite self-similar with  $f_c$  ranging from 7.5 to 10 Hz; the largest  $M_L$  4.4 mainshock showing the medium corner frequency. This points to quite small source areas with rupture radii in the interval from 110 to 150 m and high stress drops ranging from 20 to 120 MPa. Large stress drops exceeding 100 MPa with prevailing values 10–20 MPa have been already reported for previous swarms in this area [Michálek and Fischer, 2013]. It should be noted that the small rupture size of the mainshocks is consistent with the focal geometry where the rupture fits well in the fault step over of about 250 m (Figures 2 and 6).

We fitted a plane to the hypocenters of the 2014 earthquakes occurred deeper than 8 km. The least squares fit results in a strike of 356.0° and a dip of 85.4° for this plane. Figure 6 shows the projection of the hypocenters on this plane, color coded by their perpendicular distance. The geometrical step over of the fault at the location of the largest mainshock hypocenter is clearly visible. Furthermore, we compared the mainshock rupture plane given by the focal mechanism solution (strike = 25°, dip = 56°) with this plane fitted to the hypocenter distribution of the earthquake sequence. In particular, we similarly color coded the perpendicular offset of the mainshock rupture plane in the inset of Figure 6. It shows that the mainshock rupture plane nicely connects the location of the hypocenters of one side of the gap with those on the other side, supporting our conclusion that mainshock rupture interconnected both fault planes.

The Mohr-Coulomb diagram in Figure 5a shows the tractions for the estimated focal mechanisms of the  $M_L \geq 2$  events. Here we assumed a regional stress field characterized by azimuth/plunge of 139°/35° and 233°/6° for  $\sigma_1$  and  $\sigma_3$ , respectively, and a shape ratio of 0.8 [Wirth et al., 2000; Vavryčuk, 2014]. It appears that the fault planes of all three mainshock are strongly unfavorably oriented to the regional stress with the smallest instability value of all analyzed events.

Because of its unfavorable orientation, the fault jog likely acted as a barrier which did not rupture during previous swarm occurrences on the fault plane. However, previous activity might have facilitated the shear failure of this unfavorably oriented mainshock mechanism. To verify this, we tested a simplified model of this geometry by considering a step of a vertical fault with an offset of 300 m in fault perpendicular and 400 m in strike direction. By means of the analytic formulas for an elastic half-space [Okada, 1992; Toda et al., 2011], we found that precursory activity on both sides of the fault leads in this case to an increased Coulomb stress for the mainshock mechanism in the step over. Assuming a friction coefficient of 0.6 and two  $M_w$  3.4 events on both parts of the fault with stress drop of 20 MPa, a mean Coulomb stress increase of 0.3 MPa is found at the oblique link of the two faults. Vice versa, slip in the step over region with the mainshock mechanism is found

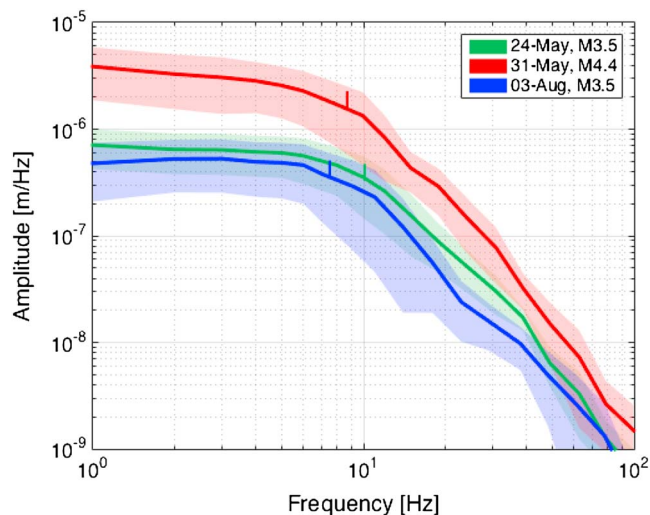


**Figure 5.** Displacement spectrum of the three mainshocks obtained as the mean value of spectra of 11 stations corrected for station-specific attenuation; shaded areas indicate the standard deviations. Corner frequencies obtained similar to Michálek and Fischer [2013] are indicated by vertical bars.

in the same model to increase the Coulomb failure stress for slip on the fault segments, as expected for static stress triggering of aftershocks [Stein, 1999].

### 3.3. Temporal Distribution

Figure 7 shows the sequences observed in the years 2008, 2011, and 2014, where each is stacked relative to the occurrence time of the largest earthquake. The comparison demonstrates that the sequence in 2014 was extraordinary in its characteristics consisting of (i) a rapid onset of the activity at the mainshock time, (ii) a strong decay of the activity after the mainshock, and (iii) a significant gap between mainshock magnitude and the magnitudes of the other events. None of these characteristics, which point to a typical mainshock-aftershock sequence, is observed for the two preceding sequences occurred in the same location. In the following, we quantify the characteristics of the 2014 seismicity in detail. Here we concentrate on the most active mainshock-aftershock sequence related to the  $M_L 4.4$  mainshock which allows a meaningful statistical evaluation.

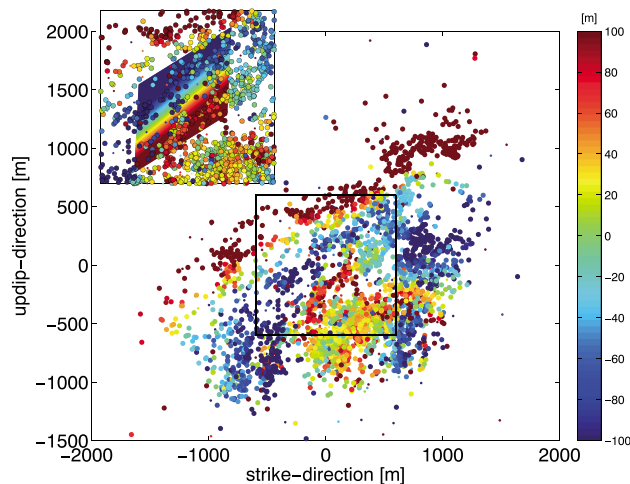


**Figure 6.** Projection of the hypocenters on the fitted plane, where the mainshock is positioned at the origin of the local coordinate system. The plane-normal distances are color coded highlighting the geometrical discontinuity in the mainshock area. Large points refer to hypocenters with location errors less than 5 m. The inset shows the region marked by the box with the surface representing the mainshock rupture plane according to the inverted focal mechanism, where colors refer to the perpendicular distance of the mainshock rupture plane to the plane fitted to the earthquake hypocenters. The mainshock rupture size corresponds to stress drop of approximately 20 MPa.

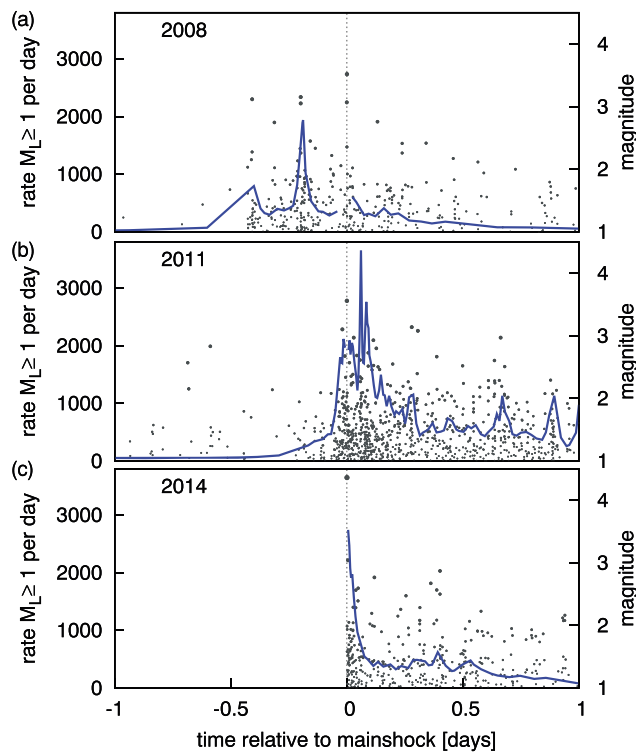


**Figure 7.** Rate of  $M_L \geq 1.0$  events (lines) as function of time relative to the largest earthquakes observed in the years (a) 2008, (b) 2011, and (c) 2014. In all plots, rates are calculated for 30 subsequent events with a step size of 10, while points indicate the magnitudes of the events with scale on right.

### 3.3.1. Omori-Type Aftershock Decay

We fitted the Omori-Utsu law (equation (1)) to the first 10 days of the  $M_L \geq 1$  aftershocks following the  $M_L 4.4$  mainshock. The maximum likelihood estimation [see, e.g., Utsu *et al.*, 1995] yields the parameters  $K_0 = 4.1 \cdot 10^4$ ,  $c = 2.0$  days, and  $p = 5.1$ . Figure 8 shows that the aftershock activity can be very well fitted after 0.3 days indicating a classical aftershock sequence. However, the aftershock productivity is found to be unusually high. To demonstrate this, we compare in Figure 8 the observed number with the Reasenberg-Jones aftershock model derived for aftershock sequences in California [Reasenberg and Jones, 1994], showing that the productivity exceeds the expectation of this standard model by more than a factor of 3. In addition to

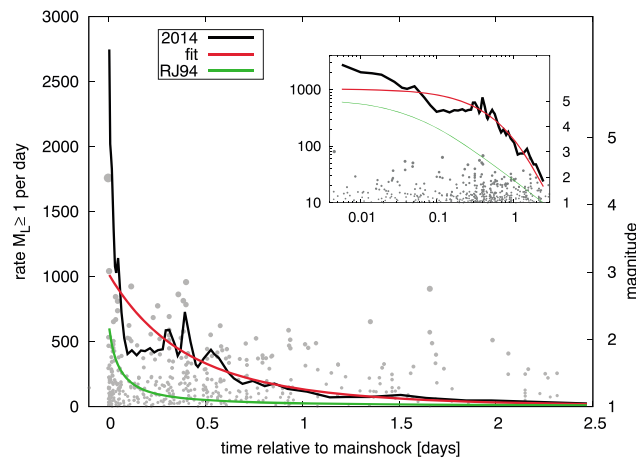


**Figure 8.** Aftershock decay following the year 2014 mainshock (see Figure 7c) in comparison to the fit of the Omori-Utsu law ( $c = 2.0$  days,  $p = 5.1$ ) and the average empirical aftershock decay in California according to the RJ94 model [Reasenberg and Jones, 1994]. The inset presents the result in double logarithmic scale.

**Table 1.** Estimated ETAS Parameters for  $M \geq 1.0$  Events Where Lowest AIC Values Indicate the Best Fit, and the Background Fraction Gives the Fraction of Aftershocks Which Are Associated to the Background Forcing<sup>a</sup>

	Background	Fraction	$K$	$c$ [s]	$\alpha$	$p$	AIC
Nonparametric	$n_{\text{opt}} = 15$	0.49	0.0038	24.2	0.35	1.46	-4076.1
... with fixed $\alpha$	$n_{\text{opt}} = 10$	0.59	0.0007	26.8	1.0	1.52	-4041.9
... with fixed $p, \alpha$	$n_{\text{opt}} = 3$	0.75	0.0025	0.3	1.0	1.0	-3999.2
Exponential fit	$0.7 + 418 \exp(-1.49t)$	0.62	0.00002	61.3	0.31	2.37	-4086.6
... with fixed $\alpha$	$0.6 + 445 \exp(-1.51t)$	0.65	0.0002	35.4	1.0	1.74	-4043.1
... with fixed $p, \alpha$	$0.0 + 498 \exp(-1.81t)$	0.59	0.0045	0.7	1.0	1.0	-3977.2
Constant	0.08	0.001	0.025	38.0	0.33	1.27	-4037.9
... with fixed $\alpha$	$\approx 0.0$	$\approx 0.0$	0.0066	28.5	1.0	1.25	-3973.4
... with fixed $p, \alpha$	$\approx 0.0$	$\approx 0.0$	0.012	2.6	1.0	1.0	-3900.6

<sup>a</sup>In the case of nonparametric fits,  $n_{\text{opt}}$  refers to the value of smoothing parameter  $n$  leading to the minimum AIC value provided in the last column.

the productivity, the shape of the decay is also unusual: The exponent  $p = 5.1$  is much higher than typical  $p$  values of aftershock sequences which are found to range in the interval 0.8–1.2 [Utsu *et al.*, 1995; Hainzl and Marsan, 2008], and the  $c$  value is much larger than the incompletely recorded time interval after the mainshock. Note that the high values are likely related to the almost constant rate of observed events within the first half-day and the trade-off between the  $c$  and  $p$  value estimation [Holschneider *et al.*, 2012]. Furthermore, secondary aftershock activity triggered by aftershocks themselves might have also affected the decay.

### 3.3.2. Aseismic Forcing

Now we test whether the observed seismicity can be solely explained by aftershock triggering, or an additional aseismic source is required to fit the activity. Here we consider the empirical observation that not only the mainshock but also aftershocks themselves can trigger Omori-Utsu-type aftershock sequences, where the productivity scales exponentially with the event magnitude. This is the basic assumption of the epidemic-type aftershock sequence (ETAS) model [Ogata, 1988], describing the seismicity rate  $R(t)$  as superposition of a constant (tectonic) background rate  $\mu$  and aftershock rates according to

$$R(t) = \mu(t) + \sum_{i: t_i < t} K 10^{\alpha(M_i - M_c)} (c + t - t_i)^{-p}, \quad (2)$$

where  $t_i$  and  $M_i \geq M_c$  are the occurrence times and local magnitudes of the observed earthquakes. In the case of the occurrence of an aseismic source such as transient creep or pore pressure changes, the seismicity is additionally forced and the background rate  $\mu(t)$  becomes time dependent [Hainzl and Ogata, 2005]. We apply the approach of Marsan *et al.* [2013], which has been further tested and applied by Hainzl *et al.* [2013] to detect aseismic forcing, if occurred, by statistically separating  $\mu(t)$  from the activity related to earthquake-earthquake interactions. The methodology uses an iterative optimization procedure to estimate the triggering parameters  $K, \alpha, c$ , and  $p$  and the background rate  $\mu(t)$  simultaneously via maximum likelihood estimation. In each iteration, the probability of every event to be triggered by the background rate is determined by  $\mu(t)/R(t)$  [Zhuang and Ogata, 2004]. Then  $\mu(t)$  is recalculated at the occurrence time of events based on these probabilities and the time interval of the  $\pm n$  neighbors. Thus,  $n$  defines the smoothing window of the  $\mu(t)$  estimate. The algorithm is iterated until convergence, and the optimal smoothing parameter  $n$  is determined by the Akaike Information Criterion (AIC).

We apply this method to the earthquake sequence of  $M_L \geq M_c = 1$  events of the mainshock sequence in the time interval  $[-1, 10]$  days relative to the  $M_L 4.4$  event, ignoring the time period directly after the occurrence of the mainshock which is potentially incomplete according to the empirical relation of Helmstetter *et al.* [2006]. The result shows (Table 1) that the best fit with minimum AIC is obtained for transient aseismic forcing with optimal smoothing parameter of  $n = 15$  neighbors. The corresponding ETAS parameters yield now a small  $c$  value (approximately 30 s) and  $p = 1.46$  as shape parameters of the Omori-Utsu law. The latter is still higher than 1 but close to typical values, while the inverted  $\alpha$  value of 0.35 is significantly smaller than those values observed for typical aftershock sequences. However, smaller  $\alpha$  values have been previously found to be indicative for swarm activity.

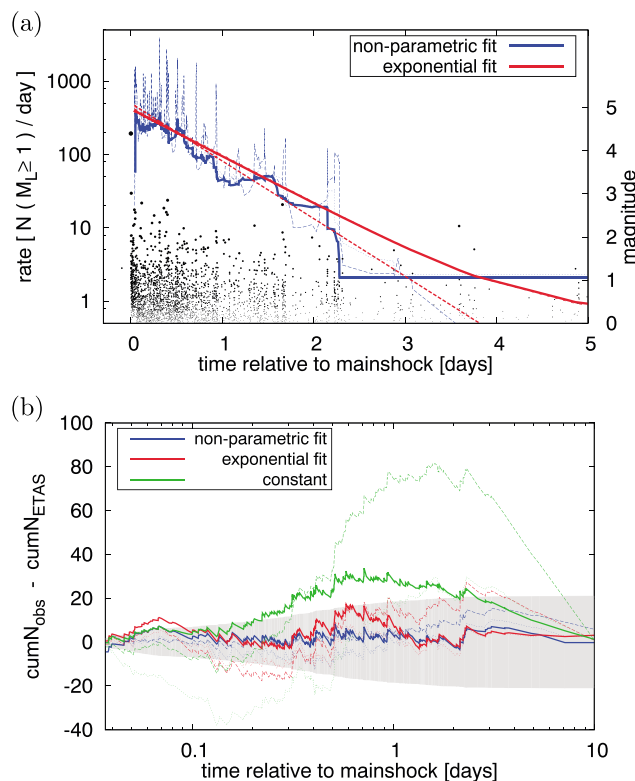


**Figure 9.** ETAS fit as function of time: (a) Inverted background rate and occurred earthquakes (points) with magnitude scale on the right. (b) The difference between the observed and modeled cumulative number of  $M_L \geq 1$  aftershocks, where the potentially incomplete time period directly after the mainshock ([0, 0.034] days) is ignored in both cases. Results are shown for the ETAS model (equation (2)) with nonparametric (blue), exponential function (red), and constant (green) background rate, where solid lines refer to the fit with all parameters while dotted and dashed curves refer to the results with fixed  $\alpha = 1$  and  $p = \alpha = 1$ , respectively. Note that the values of the estimated constant background rate are not shown in Figure 9a but can be found in Table 1. The shaded gray area in Figure 9b refers to  $\pm 1$  standard deviation assuming a Poisson distribution with the observed number of events.

To check the influence of these parameters, we additionally performed the maximum likelihood fit with fixed  $\alpha$  or/and  $p$  values set to typical values at tectonic plate boundaries ( $\alpha = p = 1.0$ ). The results show that in all cases, a time-dependent background rate is also clearly preferred indicated by AIC values which are at least 38 units smaller than the corresponding values for the ETAS model with constant  $\mu$  (which is also shown in Table 1). However, the model with free  $p$  and  $\alpha$  values gives a significantly better fit based on the AIC values. In all cases, the aseismic forcing is identified to have triggered a substantial part of the observed seismicity. In particular, the estimated fraction of earthquakes associated to the aseismic transient source is found to range between 50% and 75% of the total activity. Besides more reasonable Omori-Utsu parameters, the transient aseismic forcing can thus also explain the unusually high aftershock productivity.

The inverted background rates are shown by blue lines in Figure 9a. To evaluate the quality of the corresponding fit of the ETAS model, Figure 9b shows, as function of time, the difference between the observed cumulative number of  $M_L \geq 1$  events and that expected by the ETAS model (i.e., integration of equation (2)). The visual comparison shows that the ETAS model with time-dependent background fits the observation well, while the standard ETAS model with constant background results in strong deviations. Interestingly, the estimated time-dependent aseismic rates seem to follow approximately an exponential decay corresponding to a linear decay in the semilogarithmic plot of Figure 9a. Thus, we directly test a model with parameterized exponential background rate in the form  $\mu(t) = \mu_0 + c_1 e^{-c_2 t}$ . It turns out that this model is preferred based on the AIC value which is smaller than that of the best nonparametric version of  $\mu(t)$  (Table 1 and red lines in Figure 9). While the absolute fit (likelihood value) is slightly worse in the case of the exponential model, the number of free parameters is significantly reduced, and thus, it is preferred by the information criteria, compliant with the Occam's razor principle. Accordingly, this result leads to the conclusion that an aseismic

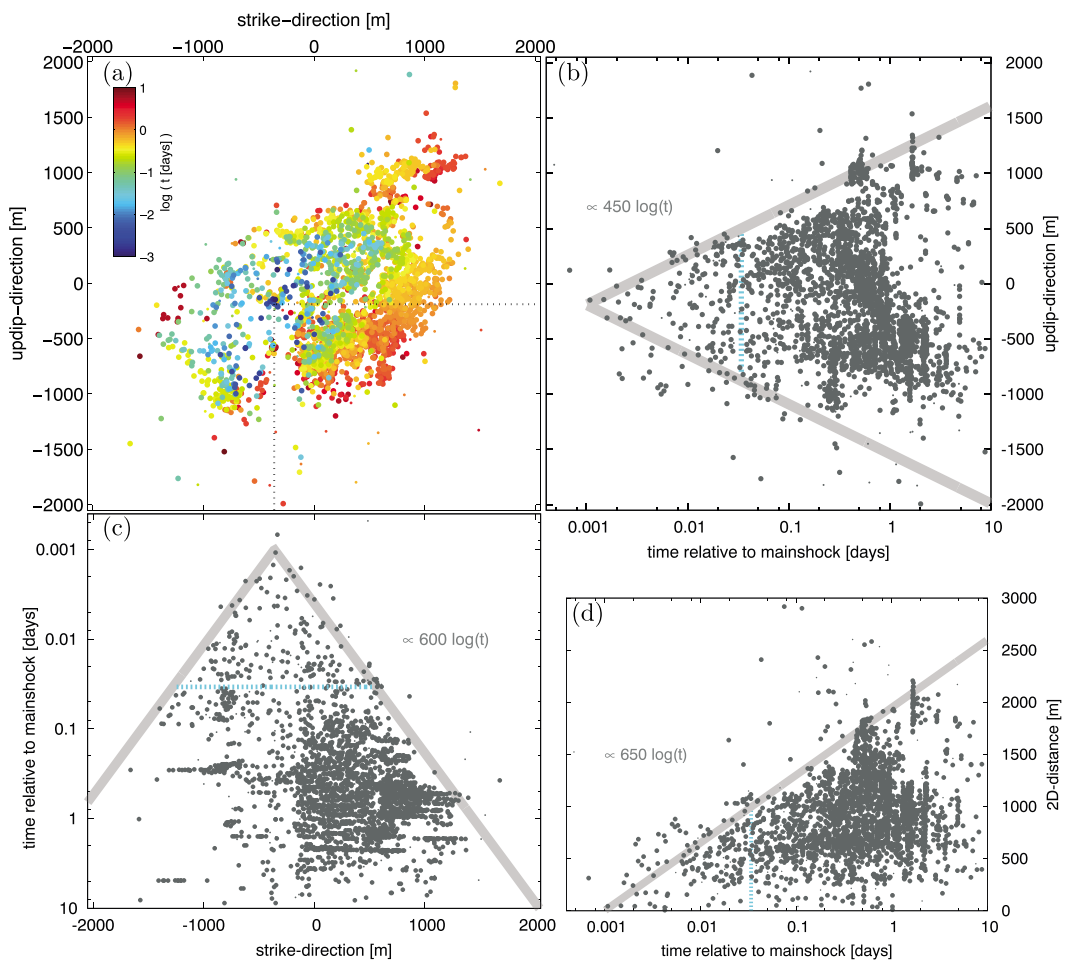


**Figure 10.** Migration of the first 10 days aftershock activity following the  $M_{4.4}$  mainshock: (a) Hypocenters projected on the plane with colors referring to the time relative to the mainshock. (b and c) The locations are shown as a function of time relative to the mainshock in strike and dip direction. Note that the mainshock occurred at the origin of the local coordinate system. (d) The 2-D distances measured to the reference point marked in Figure 10a by dotted lines. Large points indicate hypocenters with location errors  $\leq 5$  m. Gray lines refer to the functional growth denoted in the corresponding plots. The dashed lines in Figures 10b and 10c indicate the end of the first 0.034 days period which is likely incomplete. The catalog incompleteness might explain the sparser density of locations in the first period.

process has been initiated at the same time as the mainshock with a triggering potential that decayed approximately exponentially in time.

### 3.4. Spatiotemporal Migration

In addition to the inverted temporal signal of the aseismic source, the spatiotemporal migration of the hypocenters can help to reveal the underlying process. In Figure 10a, the projections of all hypocenters on the fitted plane are color coded according their occurrence times. A clear spreading of the hypocenters is visible, which becomes even clearer by analyzing the in-plane distances. In Figures 10b and 10c, the spatial distances relative to the  $M_{4.4}$  hypocenter are shown as a function of  $\log(t)$  for the dip and strike direction. A clear symmetrical and approximately linear growth is observed in both directions. Such a  $\log(t)$  expansion of the aftershock zone has been previously observed for the early aftershocks of the 2014  $M_6$  Parkfield event [Peng and Zhao, 2009]. It has also been forecasted for faults governed by rate-state-dependent friction, where the rupture of the mainshock asperity triggers postseismic creep in the surrounding velocity-strengthening region (creep zone). Simulations show that this creep leads to a  $\log(t)$  migration front of aftershocks which are triggered in smaller embedded asperities [Kato, 2007]. However, in contrast to these simulations and the Parkfield case, the migration seems to start in our case from a point (or areal source with small dimension) and the final extension of the hypocenters is several times larger than in the beginning. The central point of this migration is located 360 m south and 190 m downdip of the mainshock hypocenter, which is on the left end

of the mainshock rupture plane plotted in the inset of Figure 6. While the simulations with expanding creep show only an approximately twofold increase of the initial source radius within the first 10 days [Kato, 2007], based on the source radius estimate of 130 m, the increase is significantly larger (at least tenfold) in our case. In the following, we thus provide an alternative explanation of the observed migration pattern by means of poroelastic stress changes related to fluid intrusion, which might also be applicable for sequences observed in other places in the world.

### 3.5. Pore Pressure Modeling

The area of interest is typified by strong CO<sub>2</sub> degassing; the total flow rate in mofettes and mineral springs is estimated more than 500 m<sup>3</sup>/h [Geissler *et al.*, 2005]. The isotopic signatures of He and C show mantle origin of the gas [e.g., Braeuer *et al.*, 2007], which indicates its possible involvement in the faulting process. Further indications of the role of fluids came from the analysis of the spatiotemporal patterns of previous swarms showing clear hypocenter migration and reloading [Parotidis *et al.*, 2003; Hainzl *et al.*, 2012]. An intrusion of fluids or magma has thus been suggested to be a driving force of previous activity in this region. New evidence for the involvement of fluids in local seismicity triggering comes from the observation of a sudden increase of CO<sub>2</sub> flow in a nearby mofette during the studied sequence of 2014 (J. Heinicke, personal communication, 2015). Accordingly, we try to model the migration of the aftershock hypocenters by pore pressure changes related to an intrusion of fluids, starting with the occurrence of the  $M_L$  4.4 mainshock. For that, we use the knowledge that the rate of events triggered in the whole activated area is generally proportional to the flow rate in the case of fluid injections based on theoretical reasoning and empirical observations [Shapiro *et al.*, 2013; McGarr, 2014]. Combining this assumption with our ETAS-based observation that the earthquake rate related to the aseismic source decayed exponentially with time after the mainshock, the injection flow rate should be an exponential function. Note that such an exponentially decaying flow rate is expected for the successive emptying of an overpressured fluid reservoir. We assume that the corresponding fluid migration is then limited to a rather thin damage zone of the fault, leading to a quasi two-dimensional pore pressure diffusion. In particular, based on the results of ETAS modeling, we assume, according to above consideration, that fluid intrusion starts at time  $t = 0$  (mainshock time) with a flow rate  $q(t) = C \exp(-1.5t)$  (see Table 1) at the central point of the migration patterns (see Figure 10). For simplicity, we set the initial flow to  $C = 1$  L/s. Integration of the flow rate over time leads to a total injected volume of 58 m<sup>3</sup>, which is rather small compared to volumes injected by humans, e.g., in scientific experiments at KTB (200 m<sup>3</sup>), hydraulic fracturing ( $\sim 10^4$  m<sup>3</sup>), or waste water disposals ( $10^4$ – $10^6$  m<sup>3</sup>) [McGarr, 2014]. However, all resulting pressures would be simply scaled by  $C$  if this proportionality factor is set to another value.

In the case of instantaneous triggering and uniformly distributed criticality values (i.e., the differences between the stress state and the instability threshold), the rate of triggered earthquakes in a particular location is expected to be proportional to the rate of Coulomb stress increase,  $dCFS/dt \sim dp/dt$ , considering a simple clock advance [Hainzl *et al.*, 2010]. Note that this is in agreement with the assumption that the total seismicity rate is proportional to the flow rate, because the spatial integration of the solution of  $dp/dt$  can be shown to yield a constant which is proportional to the flow rate in the case of the analytic solution of  $p(r, t)$  in response to a step change of the flow rate [Rudnicki, 1986; Segall and Lu, 2015]. As function of the distance  $r$  to the injection point, the affected area increases with the distance  $r$ ; in particular, in case of a 2-D fault zone, the area  $A$  of an annulus with mean radius of  $r$  and a width of  $\Delta$  is  $A = 2\pi r\Delta$  and thus proportional to  $r$ . Assuming a spatially uniform distribution, the number of nucleation sites  $N$  is consequently assumed to linearly increase with the value of  $r$ ,  $N \propto r$ . Thus, the total rate of triggered earthquakes at distance  $r$  is expected to be proportional to  $r \cdot dp/dt$ .

We utilize the analytic solution for the pore pressure evolution in a poroelastic medium in response to a step change of the flow rate [Rudnicki, 1986; Segall and Lu, 2015] by discretizing  $q(t)$  in time steps of 0.001 days and summing the analytic solution for the corresponding step changes of the flow rate. Here we assumed the same parameters as Segall and Lu [2015] for the drained and undrained Poisson's ratios ( $\nu = 0.25$ ,  $\nu_u = 0.3$ ), the shear modulus (20 GPa), and the Biot coefficient (0.31). The hydraulic diffusivity  $D$  is left as the only free fitting parameter.

For  $D = 10$  m<sup>2</sup>/s, the pressure expansion is found to be in good agreement with the observed hypocenter distances relative to the central point of the aftershock sequence. The corresponding pore pressure field  $p(r, t)$  is shown in Figure 11a, and  $r \cdot dp/dt$  is compared in Figure 11b to the occurrences of the observed events. The result shows that the apparent  $\log(t)$  migration is reproduced in its main parts: The onset as well as the stop

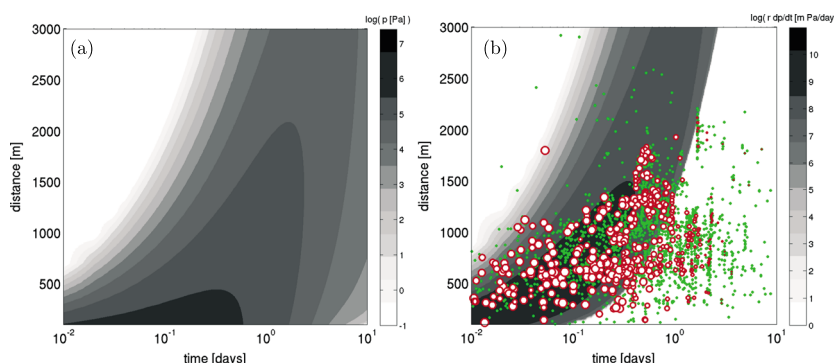


**Figure 11.** (a) Pore pressures as a function of time resulting from an injection with exponentially decaying flow rate in a fault zone with hydraulic diffusivity of  $D = 10 \text{ m}^2/\text{s}$ . (b) Time derivative of the pressure scaled by distance,  $r \cdot dp/dt$ , where small green crosses refer to  $M_L < 1$  events and red circles refer to  $M_L \geq 1$  events with size proportional to the ETAS-determined probability to be triggered by the aseismic source and not by precursory earthquakes.

of activity at different distances corresponds well with the field of positive pore pressure change (Figure 11b), despite from our simplified approximations. For example, a finite source of radius 300 m would simply shift the calculated pressure field by 300 m which would even better fit. Nevertheless, the simple model already explains most of the activity. In Figure 11b, the scaled pressure increase rates are particularly compared to the ETAS-based probability of the events to be triggered by the background rate which is here related to the pressure changes. For  $M_L \geq 1$  events, the symbol size represents this probability which is given as the ratio of the background rate to the total seismicity rate by  $\mu(t)/R(t)$  [Zhuang and Ogata, 2004] and calculated for the parameters of our best fitting ETAS model (equation (2)), namely, the model with exponential aseismic forcing (see Table 1). A good agreement between the  $r \cdot dp/dt$  field and the probability to be triggered by the aseismic source is found. In particular, the majority of earthquakes associated to the aseismic source occur where the pore pressure model predicts high rates. In contrast, events occurred where  $r \cdot dp/dt$  predicts low external forcing are very likely triggered by the mainshock or its aftershocks according to the result of the ETAS model. Anyway, some late events could be also directly explained by pore pressure changes, if some delayed triggering mechanism applies such as rate-and-state-dependent nucleation [Dieterich, 1994].

#### 4. Discussion and Conclusions

We analyzed the mainshock-aftershock sequences occurred in May–August 2014 in West Bohemia/Vogtland in order to reveal the origin of this type of seismicity in a typical location of repeated swarm activity. Our detailed investigation of the  $M_L 4.4$  sequence uncover some important characteristics:

- The mainshock occurred at a fault jog and its rupture showed the most unfavorable orientation to the regional stress field of all the analyzed events. It has interconnected two preexisting parallel fault segments activated by aftershocks whose ruptures were optimally oriented.
- The aftershock decay is anomalous in its high activity level and its shape, which is both explained by the identified strong aseismic driving force which decayed almost exponentially since the mainshock and triggered the majority of aftershocks.
- The striking migration patterns of the aftershocks can be well modeled by pore pressure diffusion along a 2-D fault due to fluid intrusion.

Accordingly, we interpret the mainshock-aftershock sequence as a result of combined action of tectonic stress, Coulomb stress change due to mainshock rupture, and migration of overpressurized fluids along the preexisting fault planes. This is supported by the following independent reasoning: To bring the unfavorably oriented mainshock rupture to failure requires the decrease of the effective normal stress, most likely by high fluid pressure. Furthermore, the detected aseismic forcing according to an exponential function is characteristic for emptying a pressurized fluid reservoir, which has been opened by the mainshock rupture. Finally, pore pressure diffusion in response to an exponentially decaying injection rate gives excellent prediction of the observed spatiotemporal evolution of aftershock hypocenters, particularly of those events associated to background forcing.

The presence of pressurized fluids (most probably CO<sub>2</sub>) in the faults in West Bohemia/Vogtland has been suggested before by various studies. By analyzing the moment tensors of the 1997 swarm and the corresponding fault tractions, Vavryčuk [2002] has estimated the fluid pressure acting on the fault was almost lithostatic. Hainzl *et al.* [2012] has attributed the vertical asymmetry of the hypocenter migration during the 2008 swarm to driving stress gradients, which allowed to estimate that the injection pressure responsible for driving the activity exceeded the minimum stress component by about 20 MPa. Also, in other regions, the release of crustal fluids has been previously identified to trigger seismicity, e.g., during the 1997 Umbria-Marche sequence [Miller *et al.*, 2004] and after the 2009 L'Aquila earthquake [Chiarabba *et al.*, 2015]. Evidence comes also from strong earthquakes as in the case of 2008 Wenchuan  $M_s$ 8.0 [Liu *et al.*, 2014] and 2011 Tohoku-oki  $M_w$ 9.0 [Terakawa *et al.*, 2013] mainshocks, whose aftershocks were, based on pore pressure diffusion and Coulomb failure analysis, partly driven by an increase of fluid pressure in the fault.

The occurrence of classical mainshock-aftershock sequences in a location of repeated swarm activity as reported in our study raises the general question about the generation mechanism of swarm and mainshock-aftershock sequences. Can a fault zone undergo a system change with time from swarm-type to main shock-aftershock-type seismic energy release? If yes, this could have important implications for the regional seismic hazard assessment. However, our study shows that this is probably not the case in the source region of Nový Kostel. The occurrence of the mainshocks seems to be related to the geometrical step over of the fault plane, which is less favorably oriented to the regional stress field than in-plane activity, explaining why it has not been ruptured during previous swarms. However, the mainshock was likely facilitated by positive static stress transfers from precursory swarm activity and finally failed. Its rupture seemed to open a fluid pathway connecting hydraulically a high-pressure source with the fault zone leading to a fluid intrusion with exponentially decreasing rate due to a limited source volume. In addition to the static stress changes of the mainshock, the pressure changes associated to the fluid intrusion likely triggered the observed seismicity in the fault plane. This explains the migration patterns as well as the unusual productivity and shape parameters of the observed Omori-Utsu aftershock decay.

#### Acknowledgments

We are grateful to the Editor Yehuda Ben-Zion, the anonymous Associate Editor, and two reviewers for their helpful suggestions. This work was supported by the grant project P210/12/2336 of the Grant Agency of the Czech Republic, and the monitoring system WEBNET providing earthquake data was supported by the Ministry of Education, Youth, and Sport of the Czech Republic (project LM2010080). The authors thank Josef Horálek for providing the waveform data of the WEBNET [*Institute of Geophysics*, 1991] seismic network. For the relocated earthquake catalog and obtained focal mechanisms, please contact Tomas Fischer (fischer@natur.cuni.cz).

#### References

- Braeuer, K., H. Kaempf, U. Koch, S. Niedermann, and G. Strauch (2007), Seismically induced changes of the fluid signature detected by a multi-isotope approach (He, CO<sub>2</sub>, CH<sub>4</sub>, N<sub>2</sub>) at the Wettingquelle, Bad Brambach (central Europe), *J. Geophys. Res.*, 112, B04307, doi:10.1029/2006JB004404.
- Báth, M. (1965), Lateral inhomogeneities in the upper mantle, *Tectonophysics*, 2, 483–514, doi:10.1016/0040-1951(65)90003-X.
- Čermáková, H., and J. Horálek (2015), The 2011 West Bohemia (Central Europe) earthquake swarm compared with the previous swarms of 2000 and 2008, *J. Seismol.*, 19, 899–913, doi:10.1007/s10950-015-9502-3.
- Chiarabba, C., P. De Gori, and P. M. Mele (2015), Recent seismicity of Italy: Active tectonics of the central Mediterranean region and seismicity rate changes after the  $M_w$ 6.3 L'Aquila earthquake, *Tectonophysics*, 638, 82–93, doi:10.1016/j.tecto.2014.10.016.
- Chiariuice, L. (2012), Unravelling the complexity of Apenninic extensional fault systems: A review of the 2009 L'Aquila earthquake (Central Apennines, Italy), *J. Struct. Geol.*, 42, 2–18, doi:10.1016/j.jsg.2012.06.007.
- Courboulex, F., A. Dujardin, M. Vallee, B. Delouis, C. Sira, A. Deschamps, L. Honore, and F. Thouvenot (2013), High-frequency directivity effect for an  $M_w$  4.1 earthquake, widely felt by the population in southeastern France, *Bull. Seismol. Soc. Am.*, 103, 3347–3353.
- Dieterich, J. H. (1994), A constitutive law for rate of earthquake production and its application to earthquake clustering, *J. Geophys. Res.*, 99, 2601–2618.
- Duverger, C., M. Godano, P. Bernard, and H. Lyon-Caen (2015), The 2003–2004 seismic swarm in the western Corinth rift: Evidence for a multiscale pore pressure diffusion process along a permeable fault system, *Geophys. Res. Lett.*, 42, 7374–7382, doi:10.1002/2015GL065298.
- Enescu, B., J. Mori, and M. Miyazawa (2007), Quantifying early aftershock activity of the 2004 mid-Niigata Prefecture earthquake ( $M_w$ 6.6), *J. Geophys. Res.*, 112, B04310, doi:10.1029/2006JB004629.
- Fischer, T. (2003a), Automatic location of swarm earthquakes from local network data, *Stud. Geophys. Geod.*, 47, 83–98.
- Fischer, T. (2003b), The August–December 2000 earthquake swarm in NW Bohemia: The first results based on automatic processing of seismograms, *J. Geodyn.*, 35(1–2), 59–81.
- Fischer, T., J. Horálek, J. Michálek, and A. Boušková (2010), The 2008-West Bohemia earthquake swarm in the light of the WEBNET network, *J. Seismol.*, 14, 665–682.
- Fischer, T., J. Horálek, P. Hrubcová, V. Vavryčuk, K. Braeuer, and H. Kaempf (2014), Intra-continental earthquake swarms in West Bohemia and Vogtland: A review, *Tectonophysics*, 611, 1–27, doi:10.1016/j.tecto.2013.11.001.
- Geissler, W., H. Kämpf, R. Kind, K. Braeuer, K. Klinge, T. Plenefisch, J. Horálek, J. Zedník, and V. Nehyba (2005), Seismic structure and location of a CO<sub>2</sub> source in the upper mantle of the western Eger (Ohre) Rift, central Europe, *Tectonics*, 24, TC5001, doi:10.1029/2004TC001672.
- Hainzl, S., and T. Fischer (2002), Indications for a successively triggered rupture growth underlying the 2000 earthquake swarm in Vogtland/NW Bohemia, *J. Geophys. Res.*, 107(B12), 2338, doi:10.1029/2002JB001865.
- Hainzl, S., and D. Marsan (2008), Dependence of the Omori-Utsu law parameters on mainshock magnitude: Observations and modeling, *J. Geophys. Res.*, 113, B10309, doi:10.1029/2007JB005492.
- Hainzl, S., and Y. Ogata (2005), Detecting fluid signals in seismicity data through statistical earthquake modeling, *J. Geophys. Res.*, 110, B05S07, doi:10.1029/2004JB003247.
- Hainzl, S., G. B. Brietzke, and G. Zöller (2010), Quantitative earthquake forecasts resulting from static stress triggering, *J. Geophys. Res.*, 115, B11311, doi:10.1029/2010JB007473.

- Hainzl, S., T. Fischer, and T. Dahn (2012), Seismicity-based estimation of the driving fluid pressure in the case of swarm activity in Western Bohemia, *Geophys. J. Int.*, 191, 271–281.
- Hainzl, S., O. Zákhrova, and D. Marsan (2013), Impact of aseismic transients on the estimation of aftershock productivity parameters, *Bull. Seismol. Soc. Am.*, 103, 1723–1732, doi:10.1785/0120120247.
- Helmstetter, A., Y. Y. Kagan, and D. D. Jackson (2006), Comparison of short-term and time-independent earthquake forecast models for southern California, *Bull. Seismol. Soc. Am.*, 96(1), 90–106.
- Holschneider, M., C. Narteau, P. Shebalin, Z. Peng, and D. Schorlemmer (2012), Bayesian analysis of the modified Omori law, *J. Geophys. Res.*, 117, B06317, doi:10.1029/2011JB009054.
- Horálek, J., T. Fischer, P. Einarsson, and S. Jakobsson (2015), Earthquake swarms, in *Encyclopedia of Earthquake Engineering*, edited by M. Beer et al., pp. 1–16, Springer, Berlin, doi:10.1007/978-3-642-36197-5\_294-1.
- Institute of Geophysics, A. o. s. o. t. C. R. (1991), West Bohemia local seismic network, International Federation of Digital Seismograph Networks, Other/Seismic Network, doi:10.7914/SN/WB.
- Kagan, Y. Y. (2004), Short-term properties of earthquake catalogs and models of earthquake source, *Bull. Seismol. Soc. Am.*, 94(4), 1207–1228.
- Kato, N. (2007), Expansion of aftershock areas caused by propagating post-seismic sliding, *Geophys. J. Int.*, 168, 797–808.
- Lay, T., and T. C. Wallace (1995), *Modern Global Seismology*, Academic Press, San Diego, Calif.
- Lengliné, O., and J.-P. Ampuero (2015), Insights on earthquake triggering processes from early aftershocks of repeating micro-earthquakes, *J. Geophys. Res. Solid Earth*, 120, 6977–6992, doi:10.1002/2015JB012287.
- Liu, Y., T. Chen, F. Xie, F. Du, D. Yang, L. Zhang, and L. Xu (2014), Analysis of fluid induced aftershocks following the 2008 Wenchuan  $M_s$  8.0 earthquake, *Tectonophysics*, 619–620, 149–158, doi:10.1016/j.tecto.2013.09.010.
- Lohman, R. B., and J. J. McGuire (2007), Earthquake swarms driven by aseismic creep in the Salton Trough, California, *J. Geophys. Res.*, 112, B04405, doi:10.1029/2006JB004596.
- Marsan, D., E. Prono, and A. Helmstetter (2013), Monitoring aseismic forcing in fault zones using earthquake time series, *Bull. Seismol. Soc. Am.*, 103(1), 169–179.
- McGarr, A. (2014), Maximum magnitude earthquakes induced by fluid injection, *J. Geophys. Res. Solid Earth*, 119, 1008–1019, doi:10.1002/2013JB010597.
- Michálek, J., and T. Fischer (2013), Source parameters of the swarm earthquakes in West Bohemia/Vogtland, *Geophys. J. Int.*, 195, 1196–1210.
- Miller, S. A., C. Collettini, L. Chiaraluce, M. Cocco, M. Barchi, and B. J. P. Kaus (2004), Aftershocks driven by a high-pressure CO<sub>2</sub> source at depth, *Nature*, 427, 724–727.
- Mogi, K. (1963), Some discussions on aftershocks, foreshocks and earthquake swarms—The fracture of a semi-infinite body caused by an inner stress origin and its relation to the earthquake phenomena (third paper), *Bull. Earthquake Res. Inst. Univ. Tokyo*, 41, 615–658.
- Neunhöfer, H., and A. Hemmann (2005), Earthquake swarms in the Vogtland/Western Bohemia region: Spatial distribution and magnitude-frequency distribution as an indication of the genesis of swarms?, *J. Geodyn.*, 39, 361–385.
- Nur, A., and J. R. Booker (1972), Aftershocks caused by pore fluid flow?, *Science*, 175, 885–887.
- Ogata, Y. (1988), Statistical models for earthquake occurrence and residual analysis for point processes, *J. Am. Stat. Assoc.*, 83, 9–27.
- Ohmi, S., K. Watanabe, T. Shibutani, N. Hirano, and S. Nakao (2002), The 2000 Western Tottori earthquake—Seismic activity revealed by the regional seismic networks, *Earth Planets Space*, 54, 831–845.
- Okada, Y. (1992), Internal deformation due to shear and tensile faults in a half-space, *Bull. Seismol. Soc. Am.*, 82, 1018–1040.
- Parotidis, M., E. Rothert, and S. A. Shapiro (2003), Pore-pressure diffusion: A possible triggering mechanism for the earthquake swarms 2000 in Vogtland/NW-Bohemia, central Europe, *Geophys. Res. Lett.*, 30(20), 2075, doi:10.1029/2003GL018110.
- Peng, Z. G., J. E. Vidale, and H. Houston (2006), Anomalous early aftershock decay rate of the 2004  $M_w$  6.0 Parkfield, California, earthquake, *Geophys. Res. Lett.*, 33, L17307, doi:10.1029/2006GL026744.
- Peng, Z., and P. Zhao (2009), Migration of early aftershocks following the 2004 Parkfield earthquake, *Nat. Geosci.*, 2, 877–881.
- Perfettini, H., and J.-P. Avouac (2004), Postseismic relaxation driven by brittle creep: A possible mechanism to reconcile geodetic measurements and the decay rate of aftershocks, application to the Chi-Chi earthquake, Taiwan, *J. Geophys. Res.*, 109, B02304, doi:10.1029/2003JB002488.
- Reasenberg, P. A., and L. M. Jones (1994), Earthquake aftershocks: Update, *Science*, 265, 1251–1252.
- Rudnicki, J. W. (1986), Fluid mass sources and point forces in linear elastic diffusive solids, *Mech. Mater.*, 5(4), 383–393.
- Segall, P., and S. Lu (2015), Injection-induced seismicity: Poroelastic and earthquake nucleation effects, *J. Geophys. Res. Solid Earth*, 120, 5082–5103, doi:10.1002/2015JB012060.
- Shapiro, S. A., C. Krüger, and C. Dinske (2013), Probability of inducing given-magnitude earthquakes by perturbing finite volumes of rocks, *J. Geophys. Res. Solid Earth*, 118, 3557–3575, doi:10.1002/jgrb.50264.
- Shelly, D. R., T. A. Taira, S. G. Prejean, D. P. Hill, and D. S. Dreger (2015), Fluid-faulting interactions: Fracture-mesh and fault-valve behavior in the February 2014 Mammoth Mountain, California, earthquake swarm, *Geophys. Res. Lett.*, 42, 5803–5812, doi:10.1002/2015GL064325.
- Stein, R. S. (1999), The role of stress transfer in earthquake occurrence, *Nature*, 402, 605–609.
- Terakawa, T., C. Hashimoto, and M. Matsuzuka (2013), Changes in seismic activity following the 2011 Tohoku-oki earthquake: Effects of pore fluid pressure, *Earth Planet. Sci. Lett.*, 365, 17–24, doi:10.1016/j.epsl.2013.01.017.
- Toda, S., R. S. Stein, V. Sevilgen, and J. Lin (2011), Coulomb 3.3 graphic-rich deformation and stress-change software for earthquake, tectonic, and volcano research and teaching user guide, *U.S. Geol. Surv. Open-File Rep. 2011-1060*, p. 63, U.S. Geol. Surv., Reston, Va.
- Utsu, T., Y. Ogata, and R. S. Matsuzuka (1995), The centenary of the Omori formula for a decay law of aftershock activity, *J. Phys. Earth*, 43, 1–33.
- Vavryčuk, V. (2002), Non-double-couple earthquakes of January 1997 in West Bohemia, Czech Republic: Evidence of tensile faulting, *Geophys. J. Int.*, 149, 364–373.
- Vavryčuk, V. (2009), *The Amplitude Moment Tensor Inversion—Program AMT, Comput. Codes Lib.*, Inst. of Geophys., Prague.
- Vavryčuk, V. (2014), Iterative joint inversion for stress and fault orientations from focal mechanisms, *Geophys. J. Int.*, 199, 69–77, doi:10.1093/gji/ggu224.
- Vidale, J. E., and P. M. Shearer (2006), A survey of 71 earthquake bursts across southern California: Exploring the role of pore fluid pressure fluctuations and aseismic slip as drivers, *J. Geophys. Res.*, 111, B05312, doi:10.1029/2005JB004034.
- Waldhauser, F. (2001), hypoDD: A computer program to compute double-difference hypocenter locations, *U.S. Geol. Surv. Open File Rep. 01113*, pp. 1–25, U.S. Geol. Surv., Menlo Park, Calif.
- Waldhauser, F., and W. Ellsworth (2000), A double-difference earthquake location algorithm: Method and application to the northern Hayward fault, California, *Bull. Seismol. Soc. Am.*, 90(6), 1353–1368, doi:10.1785/0120000006.

- Wirth, W., T. Plenefisch, K. Klinge, K. Stammle, and D. Seid (2000), Focal mechanisms and stress field in the region Vogtland/Western Bohemia, *Stud. Geophys. Geod.*, 44, 126–141.
- Zhuang, J., and Y. Ogata (2004), Analyzing earthquake clustering features by using stochastic reconstruction, *J. Geophys. Res.*, 109, B05301, doi:10.1029/2003JB002879.